JOURNAL OF AGRICULTURAL AND FOOD CHEMISTRY

Functional Structure/Activity Relationships

Structural and Biochemical Characterization of the Curcumin-Reducing Activity of CurA from Vibrio vulnificus

Soo-Bong Park, Da-Woon Bae, Nina Abigail Bagay Clavio, Lei Zhao, Chang-Sook Jeong, Bomi Choi, Stephani Joy Yarcia Macalino, Hee-Jeong Cha, Jin-Byung Park, Jun Hyuck Lee, Sang-Jip Nam, Sun Choi, Min-Kyu Kim, and Sun-Shin Cha

J. Agric. Food Chem., **Just Accepted Manuscript** • DOI: 10.1021/acs.jafc.8b03647 • Publication Date (Web): 25 Sep 2018

Just Accepted

ACS Publications

is published by the American Chemical Society. 1155 Sixteenth Street N.W., Washington, DC 20036

Structural and Biochemical Characterization of the Curcumin-Reducing Activity of CurA from *Vibrio vulnificus*

Soo-Bong Park[1,¶], Da-Woon Bae[1,¶], Nina Abigail B. Clavio[2,¶], Lei Zhao[3], Chang-Sook Jeong[4,5], Bomi Choi[1], Stephani Joy Y. Macalino[2], Hee-Jeong Cha[6], Jin-Byung Park[6], Jun Hyuck Lee[4,5], Sang-Jip Nam[1], Sun Choi[2,*], Min-Kyu Kim[3,4,*] and Sun-Shin Cha[1,*]

[1]*Department of Chemistry & Nanoscience, Ewha Womans University, Seoul 03760, Republic of Korea*

[2]*College of Pharmacy and Graduate School of Pharmaceutical Sciences, Ewha Womans University, Seoul 03760, Republic of Korea*

[3]*Biotechnology Research Division, Korea Atomic Energy Research Institute (KAERI), Jeongeup 56212, Republic of Korea*

[4]*University of Science and Technology, Daejeon, Republic of Korea*

[5]*Unit of Polar Genomics, Korea Polar Research Institute, Incheon 21990, Republic of Korea*

[6]*Department of Food Science and Engineering, Ewha Womans University, Seoul 03760, Republic of Korea*

[*]Corresponding authors: Sun Choi, Min-Kyu Kim, and Sun-Shin Cha

E-mail addresses: sunchoi@ewha.ac.kr (S.C.), mkkim@kaeri.re.kr (M.-K.K.), and chajung@ewha.ac.kr (S.-S. C)

[¶]These authors contributed equally to this work.

Running title: Structure-based characterization of CurA

ABSTRACT: Curcumin is a yellow-colored ingredient in dietary spice turmeric (*Curcuma longa* Linn). This nontoxic polyphenol has anti-tumor, anti-inflammatory, apoptotic, and anti-oxidant activities. The ingested curcumin is reduced to multihydrated forms with more potent therapeutic potentials by the curcumin reductase (CurA) from commensal *Escherichia coli*. In this study, we demonstrated that *Vibrio vulnificus* CurA (*Vv*CurA) with 87% sequence similarity to the *E. coli* CurA exhibits the curcumin-reducing activity through spectrophotometric detection of NADPH oxidation and high performance liquid chromatographic analysis of curcumin consumption and product generation. Afterward, we determined the crystal structures of *Vv*CurA and the *Vv*CurA/NADPH complex, and made the *in silico* model of the *Vv*CurA/NADPH/curcumin ternary complex through induced fit docking. Based on structural information, active site residues that play critical roles in catalysis have been identified and characterized by mutational and kinetic studies, leading us to propose the reaction mechanism of CurA.

Keywords: Curcumin-reducing enzyme; crystal structure of apo *Vv*CurA; crystal structure of the *Vv*CurA/NADPH complex; *in silico* model of the *Vv*CurA/NADPH/curcumin complex; enzyme mechanism

47 ## INTRODUCTION

48 Curcumin [(1*E*,6*E*)-1,7-bis(4-hydroxy-3-methoxyphenyl)-1,6-heptadiene-3,5-dione or
49 diferuloylmethane], a yellow pigment derived from the rhizomes of a plant (*Curcuma longa*
50 Linn), has long been used as a traditional medicine and as a preservative and coloring agent
51 in foods.[1] Extensive research during the last few decades has suggested therapeutic and
52 pharmacological potentials of curcumin as anti-inflammatory, anti-oxidant, anti-cancer, anti-
53 bacterial, and neuroprotective agents.[2-7] Various animal models and human studies proved
54 that curcumin is extremely safe even at very high doses. For example, phase I clinical trials
55 indicated that curcumin, with a high dose of 12 g per day, is well tolerated.[8] The
56 pharmacological safety and efficacy of curcumin make it a potential compound for treatment
57 and prevention of a wide variety of human diseases. However, curcumin has not yet been
58 approved as a therapeutic agent, and the poor oral absorption of curcumin in both humans and
59 animals has raised several concerns that limit its clinical impact.[9-12]

60 Curcumin is a biphenolic compound with hydroxyl groups at the ortho-position on the
61 two aromatic rings that are connected by a β-diketone bridge containing two double bonds
62 (Figure 1).[13] The diketo-group can covert to enol forms through keto-enol tautomerization.
63 Curcumin is almost insoluble in aqueous solutions but soluble in polar solvents such as
64 DMSO, methanol, ethanol, acetonitrile, and so on. At physiological pH, curcumin is unstable
65 and rapidly degraded in aqueous-organic solutions such as phosphate buffers or cell culture
66 media. The degradation products of curcumin in a phosphate buffer (pH 7.4) were first
67 reported as ferulic acid, feruloyl methane, ferulic aldehyde, vanillin, and other minor
68 products.[14-15] Recently, the major degradation product of curcumin in buffers with
69 physiological pH was identified as a bicyclopentadione which is formed by autoxidation, the
70 free radical-driven incorporation of O_2.[16-17]

71 In addition, pharmacokinetic studies of curcumin administered either orally or
72 intraperitoneally in mice or human revealed that it undergoes biological transformation
73 primarily by reduction and conjugation *in vivo*.[16-18] Consecutive reduction of the double
74 bonds results in the formation of dihydrocurcumin (DHC), tetrahydrocurcumin (THC),
75 hexahydrocurcumin (HHC), and octahydrocurcumin (OHC) (Figure S1).[19] The reduced
76 metabolites, especially THC and HHC, represent the largest portion of curcumin
77 metabolites.[20] These reduced forms can be further modified as monoglucuronide,
78 monosulfate, or mixed glucuronide/sulfate by the addition of glucuronate or sulfate.[16-18]
79 Among these curcumin metabolites, THC possesses better solubility and stability than
80 curcumin at physiological pH.[21] It was also reported that THC is more potent than curcumin
81 as to anti-inflammatory[22], anti-diabetic, and anti-hyperlipidemic activity[23], and equally potent
82 as to anti-oxidant activity.[24-25] These results suggest that THC converted from the ingested
83 curcumin *in vivo* is a more promising bioactive compound than curcumin.[26-27]

84 Sequence analyses indicated that the *curA* gene product belongs to the leukotriene B_4
85 dehydrogenases family of zinc-independent medium-chain dehydrogenases/reductases (MDR)
86 superfamily with NADP(H) as a cofactor[28-29]. In enzyme assays with various compounds
87 including curcumin, 3-octene-2-one, 3-hepten-2-one, resveratrol, and *trans*-2-octenal, *E. coli*
88 CurA displayed the highest reducing activity against curcumin with K_m and V_{max} of 0.029
89 mM and 9.35 units/mg, respectively.[27] In addition, it was revealed that the reducing activity
90 of CurA was dependent on NADPH and independent of metal ions as expected from its
91 primary structure. Based on these results, CurA was referred to as a metal-independent
92 curcumin reductase (EC 1.3.1.n3) with NADPH as a cofactor.

93 Though the enzymatic activity and biochemical characteristics of CurA have been verified,
94 the mechanisms of the dual substrate (curcumin and DHC) recognition and C=C bond

95 reduction remain unknown. The *yncB* gene product of *Vibrio vulnificus* (*Vv*CurA) is a
96 putative NADPH-binding oxidoreductase that shows 87% sequence similarity to the *E. coli*
97 CurA (*Ec*CurA). In this study, we demonstrated the curcumin-reducing activity of *Vv*CurA
98 and determined the crystal structures of *Vv*CurA and the *Vv*CurA/NADPH complex.
99 Furthermore, we made the *in silico* model of the *Vv*CurA/NADPH/curcumin ternary complex,
100 which guided us to identify catalytic residues conserved in CurA orthologues through
101 mutational studies. Consequently, the structural and biochemical characterizations presented
102 in this study will play a platform to understand curcumin-reducing enzymes in a mechanistic
103 manner.

104

105 ## MATERIALS AND METHODS

106 **Cloning, Expression, and Purification.** *Vv*CurA, the *yncB* gene product, was cloned,
107 expressed, and purified as previously described.[30] In brief, the pET-24a plasmid (Novagen)
108 harbouring the *yncB* gene of *V. vulnificus* MO6-24/O[31] was transformed into the *E. coli* strain
109 Rosetta (DE3) pLysS (Stratagene). Cells were grown to OD_{600} of approximately 0.5 in Luria-
110 Bertani media containing 50 μg/mL kanamycin (Duchefa) at 37 ºC and then 1 mM isopropyl-
111 β-D-thiogalactoside (IPTG, Duchefa) was added to overexpress *Vv*CurA. After 12 h induction
112 at 22 ºC, cells were harvested and disrupted by sonication. After centrifugation at 20,000 g
113 for 30 min at 4 ºC, supernatant fraction was loaded onto nickel-nitrilotriacetic acid column
114 (Qiagen). Further purification was performed by Q-Sepharose column (GE Healthcare) and
115 Superdex 75 HR 16/60 column (GE Healthcare). For the SeMet substituted *Vv*CurA, the *E.*
116 *coli met*$^-$ auxotropic strain B834 (DE3) (Novagen) was used as a host for plasmid
117 transformation. Cells were grown up to OD_{600} of approximately 0.5 in M9 media including
118 50 mg/L of SeMet and 50 μg/mL kanamycin at 37 ºC, and the expression was induced by 1

119 mM IPTG at 22 ºC for 12 h. The SeMet *Vv*CurA was purified as described above. The
120 purified *Vv*CurA and SeMet-*Vv*CurA in a buffer containing 20 mM Tris-HCl pH 7.5, 300 mM
121 NaCl, and 1 mM DTT were concentrated to approximately 15 mg/mL for crystallization.[30]

122

123 **Crystallization, Data Collection, and Structure Determination.** The *Vv*CurA proteins were
124 crystallized and further optimized by the micro-batch crystallization method at 22 ºC.[30,32]
125 Drops composed of 1 μL protein solution and 1 μL crystallization reagent were pipetted under
126 a layer of a 1:1 mixture of silicon oil and paraffin oil in 72-well HLA plates (Nunc). Crystals
127 were grown in a mother liquor containing 200 mM NaCl, 100 mM HEPES pH 7.5, 20% (*w/v*)
128 polyethylene glycol (PEG) 8,000, and 5% 2-methyl-2,4-pentanediol (MPD). The SeMet-
129 *Vv*CurA crystals were produced in the same crystallization solution for native *Vv*CurA
130 crystals. To make the *Vv*CurA/NADP(H) complex, 5 mM NADPH was added to the native
131 *Vv*CurA protein and then the mixture was incubated with the same crystallization solution for
132 native *Vv*CurA crystallization. The SeMet-*Vv*CurA and *Vv*CurA/NADPH complex crystals
133 were frozen at 100 K after briefly soaked in a cryo-protectant solution consisting of 20%
134 MPD, 200 mM NaCl, 100 mM MES pH 6.5, and 20% (*w/v*) PEG 8,000. A 1.85 Å resolution
135 data set for SeMet-*Vv*CurA and a 2.2 Å resolution data set for the *Vv*CurA/NADPH complex
136 were collected using an ADSC Quantum 315r CCD on beamline MXII of Australian
137 Synchrotron (Melbourne, Australia). Diffraction data were processed and scaled using *XDS*
138 and *XSCALE* from the *XDS* program suite.[33] The SeMet-*Vv*CurA crystal with two molecules
139 in the asymmetric unit belongs to the space group, $P2_12_12_1$ (a = 90.52, b = 91.56, and c =
140 104.79 Å). The *Vv*CurA/NADPH complex crystal with one molecule in the asymmetric unit
141 belongs to the primitive tetragonal space group, $P4_12_12$ (a = b = 90.14 and c = 105.61 Å). The
142 structure of the apo *Vv*CurA was determined by the single wavelength anomalous dispersion

143 (SAD) method by using selenium atoms as anomalous scatterers with AutoSol in the
144 PHENIX program suit.[34] The model building was performed using the program Coot[35] and
145 the refinement was performed with Refmac5[36] in the CCP4 program suit.[37] The geometric
146 parameters of the final model were validated using PROCHECK[38] and MolProbity.[39] The
147 crystallographic data statistics are summarized in Table 1. The final models of *Vv*CurA and
148 the *Vv*CurA/NADPH complex were deposited in the Protein Data Bank with PDB codes
149 5ZXN and 5ZXU, respectively.

150

151 **Site-directed mutagenesis.** To exploit the role of active site residues on the *Vv*CurA enzyme
152 activity and reaction mechanism, we prepared five mutant *Vv*CurA proteins (R55A, Y62A,
153 Y62F, Y251A, and Y251F) by site-directed mutagenesis. The pET-24a vector including the
154 wild-type *VvcurA* gene was used as a template, and site-directed mutagenesis was performed
155 with the QiukChange kit (Stratagene). After confirming the correct incorporation of the
156 mutation, mutant proteins were purified with the same procedure for the wild-type. The
157 primer sequences for site-directed mutagenesis are described in Table S1.

158

159 **The *in silico* model of the *Vv*CurA/NADPH/curcumin complex.**

160 *Protein and Ligand Preparation*. For the docking study, the crystal structure of the
161 *Vv*CurA/NADPH complex was prepared using the Protein Preparation Wizard in Maestro
162 v11.5 (Schrödinger, LLC). In this process, bond orders were checked, hydrogen atoms were
163 added, and the proper protonation states of the residues at pH 7.4 were assigned. The added
164 hydrogens were energy minimized using the Optimized Potential for Liquid Simulation
165 (OPLS) 3 force field until the average root-mean-square deviation converged to 0.30 Å. The

166 ligand was prepared using the LigPrep module in Maestro v11.5, where its 3D structure was
167 generated and energy minimized using the OPLS3 force field.

168 *Induced-Fit Docking*. The prepared ligand was docked into the prepared protein structure
169 using the Induced-Fit Docking (IFD) module in Maestro v11.5 with the following steps: (i)
170 the binding site grid was defined as a box (12 Å per side) enclosing important residues
171 identified in the mutation study (Arg53, Arg55, Ser61, Tyr62, and Tyr251), (ii) the ligand was
172 initially docked using Glide SP (Standard Precision) with the maximum number of poses
173 retained set to 100, (iii) residues within 5Å of the ligand were refined and side chain
174 orientations were further optimized using Prime, (iv) the ligand was re-docked within 30
175 kcal/mol of the best structure. All the calculations were accomplished on an Intel® Xeon®
176 Quad-core 2.5 GHz workstation with Linux CentOS release 6.7.

177

178 **High-performance liquid chromatography (HPLC) analysis.** A 200 μL reaction mixture
179 composed of 500 μM NADPH, 200 μM curcumin, and 500 nM *Vv*CurA in a 50 mM MES
180 (pH 6.5) buffer was incubated for 18 min and then 6 M guanidine hydrochloride (1:1 volume
181 ratio) was added to stop the reaction. Subsequently the mixture was loaded onto Luna 5u C_{18}
182 100A column (100 × 4.6 mm; Phenomenex) for HPLC analysis of reaction products. Water
183 and 100% acetonitrile were used as solvents A and B, respectively. The composition of the
184 mobile-phase at 0 min was 95% solvent A and 5% solvent B. After the percentage of solvent
185 B was gradually increased to 100% over 12.5 min, 100% solvent B was held for additional
186 2.5 min. From 15 min to 18 min, the mobile-phase was gradually changed to 100% solvent A.
187 Standard samples, THC (200 μM) and curcumin (200 μM), were also analyzed by the same
188 method. The detector wavelength was 280 nm and elution profiles were plotted using the
189 OriginPro 2018b program (OriginLab).

190

191 **Assay of enzyme activity** The *Vv*CurA activity was measured by monitoring curcumin
192 reduction with a spectrophotometer (SpectraMAX190, Molecular Devices) at room
193 temperature. After a 15-min incubation of *Vv*CurA and NADPH in a dark condition, the
194 reaction was started by adding curcumin. The assay mixture comprised 100 mM phosphate
195 buffer (pH 6.0), 5% DMSO, 150 μM NADPH, 5 μM curcumin, and native or mutant *Vv*CurA
196 proteins (50 nM) in a total volume of 200 μL. The level of curcumin reduction was measured
197 at 430 nm for 20 min with 15 sec intervals. The relative enzyme activities were quantified
198 based on a percentage according to the following equation: $(v_{\mathrm{M}}/v_{\mathrm{WT}}) \times 100$, where v_{M}
199 and v_{WT} are initial velocity of mutated and wild-type *Vv*CurA proteins, respectively.

200 Steady-state kinetic analyses were performed with various concentrations of curcumin (0-
201 100 μM) and 500 μM NADPH. The reaction buffer was composed of 100 mM phosphate (pH
202 6.0), 5% ethanol, and 3 mM hydroxypropyl β-cyclodextrin. Other reaction conditions were
203 described above. The K_{m}, V_{max}, and k_{cat} values were determined by fitting data to the
204 Michaelis–Menten equation using the OriginPro 2018b program (OriginLab). All kinetic
205 measurements were performed at least two times.

206

207 RESULTS AND DISCUSSION

208 **Curcumin-reducing activity of *Vv*CurA.** Since *Vv*CurA is a NADPH-dependent reductase
209 to convert curcumin into THC, we examined NADPH oxidation by monitoring absorbance at
210 340 nm. It should be noted that all the enzyme assays in this study were performed with
211 purified proteins. When curcumin was added to the solution containing *Vv*CurA and NADPH,
212 decrease in absorbance was observed (Figure 2A), which indicates that NADPH was oxidized

213 during the reaction. Furthermore, we verified the production of THC and the consumption of
214 curcumin with the HPLC spectra of THC and curcumin as references; when the reaction
215 mixture consisting of curcumin, *Vv*CurA, and NADPH was analyzed by reverse-phase HPLC,
216 the spectrum pattern with two peaks characteristic of THC were observed and there was no
217 peak corresponding to curcumin (Figure 2C). According to the steady-state kinetic analyses,
218 K_m, V_{max}, and k_{cat} values were 35 μM, 9.5 units/mg, and 352 min^{-1}, respectively. It is notable
219 that the K_m and V_{max} values of *Vv*CurA are comparable to those of *Ec*CurA.[27] In addition, the
220 optimal pH (~5.2) and temperature (35 ºC) of *Vv*CurA are also similar to those of *Ec*CurA
221 (Figure S2).

222

223 **Overall Structure of *Vv*CurA.** To elucidate the curcumin-reducing mechanism of *Vv*CurA,
224 we determined the crystal structures of *Vv*CurA in its apo and NADPH-bound states. The
225 1.85 Å resolution crystal structure of apo *Vv*CurA was first determined by the single-
226 wavelength dispersion method. The 2.2 Å resolution crystal structure of the *Vv*CurA/NADPH
227 complex was then determined by the molecular replacement method with the apo structure as
228 a search model. NADPH binding induces no remarkable conformational change in the
229 *Vv*CurA structure, which is well reflected in the small root-mean-square deviation (rmsd)
230 value of 0.517 Å between the crystal structures of *Vv*CurA and the *Vv*CurA/NADPH complex.

231 As shown in Figure 3A and S3, the monomer of *Vv*CurA has a two-domain modular
232 structure consisting of the catalytic domain (residues 1–128 and 309–342) and the nucleotide-
233 binding domain (residues 129–308). The catalytic domain is composed of four α-helices and
234 ten β-strands which are antiparallel except for β15. It is notable that 50.3% residues in this
235 domain are located in loop regions not in secondary structural elements (Figure S3). The high
236 loop content seems to confer structural plasticity on this domain, which allows *Vv*CurA to

237 have a curcumin-binding active site pocket whose conformation is distinctive from those of
238 other zinc-independent MDR superfamily members (See the 'Structural Comparison' section).
239 The nucleotide-binding domain adopts the Rossman fold consisting of a six-stranded parallel
240 β-sheet sandwiched by eight α-helices on both sides and provides a structural platform for
241 NADPH binding. In the complex structure, NADPH nestles in the shallow groove on the C-
242 terminal edge of the central sheet in the nucleotide domain and the lid-like catalytic domain
243 covers the bound NADPH.

244 Two monomers of *Vv*CurA form an S-shaped dimer excluding ~1953 $Å^2$ solvent
245 accessible surface area of each monomer (Figure 3B). The dimerization of *Vv*CurA is
246 achieved mainly through the nucleotide-binding domain. The dimerization motif including
247 α10 and β14 (residues 262-279) is responsible for the dimerization (Figure 3C, 3D and S3).
248 The central β-sheet of one monomer is combined with that of the other monomer in an anti-
249 parallel manner through the β14 strand at one edge of the central sheet, thereby forming an
250 extended 12-stranded β-sheet across the dimer. The two dimerization motifs form the
251 triangular dimerization core with intensive hydrophobic interactions among hydrophobic side
252 chains that are clustered inside of this core (Met263, Leu266, Met267, Leu270, and Met277)
253 (Figure 3C). The triangular dimerization core is further stabilized by polar interactions at the
254 top apex (Figure 3D). The backbone oxygen of Pro257 in one monomer forms a hydrogen
255 bond with the backbone -NH group of Asp261 in the other monomer, and the side chain of
256 Asp261 in one monomer interacts with both the backbone -NH group and the side chain of
257 Arg262 in the other monomer. The dimerization seems to be essential for the activity of
258 *Vv*CurA since the α10 helix of one monomer takes part in the construction of the active site of
259 the other monomer in the dimeric structure of *Vv*CurA (Figure 3B).

260

261 **Structural comparison and the unique active site of *Vv*CurA.** Several oxidoreductases and
262 double bond reductases were identified as structural homologues of *Vv*CurA when the
263 structure of *Vv*CurA was compared with structures in the Protein Data Bank. Even though
264 they show limited sequence identity to *Vv*CurA (~10% - ~40%), they belong to the zinc-
265 independent MDR superfamily. Proteins in the zinc-independent MDR superfamily are
266 reductases using NADP(H) as a cofactor, which is compatible with the characteristics of
267 *Vv*CurA.

268 Among the identified structural homologues, we selected the leukotriene B_4 12-
269 hydroxydehydrogenase/15-oxo-prostaglandin 13-reductase[40] (hereafter referred to as LTB_4R)
270 of guinea pig that has 42% sequence identity to *Vv*CurA for structural comparison since this
271 protein was well characterized in structural and biochemical aspects. In spite of the overall
272 resemblance, *Vv*CurA displays structural differences in the catalytic domain compared to
273 LTB_4R. The catalytic domain of *Vv*CurA is superposed onto that of LTB_4R with the rmsd
274 value of 5.22 Å for 140 aligned Cα atoms whereas the rmsd values of the nucleotide-binding
275 domain for 167 aligned Cα atoms in the superposed crystal structures between *Vv*CurA and
276 LTB_4R is 2.26 Å. The larger structural differences of the catalytic domain are reflected in the
277 low sequence identity of the catalytic domains between the two proteins: the catalytic domain
278 of *Vv*CurA shows 36.7% sequence identity to that of LTB_4R. In comparison, the two proteins
279 have higher sequence identity in the nucleotide-binding domain; the nucleotide-binding
280 domain of *Vv*CurA shows 42.8% sequence identity to that of LTB_4R.

281 The structural and sequential differences of the catalytic domain lead to the distinctive
282 active site conformation in *Vv*CurA that is adequate to accommodate curcumin (Figure 5A).
283 When the structure of the *Vv*CurA/NADPH/curcumin ternary complex is superposed onto
284 that of LTB_4R, it is apparent that there is no space for curcumin binding in the active site of

285 LTB_4R (Figure 5A). The main structural determinants constructing the curcumin-binding
286 pocket in *Vv*CurA are the Tyr62 loop (residues 51-69) and the α10 helix both of which define
287 the edges of the curcumin-binding active site pocket (Figure 3B). *Vv*CurA has a 7-residue
288 insertion in the Tyr62 loop compared to LTB_4R (Figure S3). The prolonged Tyr62 loop is
289 ordered in *Vv*CurA: the average *B*-factors of this loop (46.938 $Å^2$) is lower than that of the
290 catalytic domain (54.013 $Å^2$). Tyr62 at the tip of this loop interacts with Ile281 in the
291 nucleotide-binding domain (Figure 4B), and this hydrophobic contact attaches the Tyr62 loop
292 to the nucleotide-binding domain. In contrast, the corresponding region in LTB_4R assumes a
293 helical conformation and stays away from the nucleotide binding domain (Figure 4B).
294 Compared to LTB_4R, *Vv*CurA also has a 5-residue insertion in the α10 helix that forms the
295 bottom of the active site in *Vv*CurA (Figure 3B and S3).

296

297 **NADPH binding mode.** The NADPH binding mode in *Vv*CurA is very similar to that of
298 LTB_4R, which is compatible with their high structural similarity in the nucleotide-binding
299 domain playing a major role in NADPH binding. NADPH with the anti-configuration is
300 bound at the domain interface with the nucleotide-binding domain as the platform (Figure 5).
301 It makes direct contacts with the nucleotide-binding domain whereas it mainly forms water-
302 mediated interactions with the catalytic domain. First, we describe interactions between
303 NADPH and the nucleotide-binding domain (Figure 5). The nicotinamide (NA) ring fits into
304 a hydrophobic patch lined by side chains of six residues (Met130, Val160, Phe280, Ile281,
305 Ile282, and Phe283) and the side chain methyl group of Thr134. In addition, its amide group
306 is hydrogen bonded to the backbone -CO and -NH groups of Cys245, Phe280, and Ile282.
307 The 2′-OH and 3′-OH groups of the NA-linked ribose interact with the side chain hydroxyl
308 group of Tyr251 and the backbone -CO group of Asn223, respectively. The pyrophosphate

309 group forms multiple polar interactions with the backbone -NH groups of Ala159, Val160,
310 and Gly161. In the case of the phosphate group in the 2′-phospho ribose, it is hydrogen
311 bonded to the backbone -NH group of Gly180 and the side chains of Lys184 and His200,
312 which explains the preference of CurA for NADPH. One face of the adenine base makes
313 hydrophobic contacts with side chains of Val224 and Ile248 with while the opposite face is
314 exposed to the solvent. In addition to direct interactions, N3 and the amino group in the
315 adenine base form water-mediated interactions with the backbone -NH and -CO groups of
316 Ala155 and Ser249, respectively (Figure 5).

317 Although the catalytic domain covers the bound NADPH, it makes much fewer
318 interactions with NADPH than the nucleotide-binding domain. Only Asn331 interacts with
319 NADPH in a direct manner: the side chain amide of Asn331 makes hydrogen bonds with 3′-
320 OH of the 2′-phospho ribose and one oxygen atom of the pyrophosphate group (Figure 5).
321 Other interactions are indirect; N7 of the adenine base and pyrophosphate group form water-
322 mediated complicated interactions with the catalytic domain (Figure 5). The loose contact of
323 the catalytic domain with NADPH suggest that the domain could move away from the bound
324 nucleotide to assume an open conformation, which would allow the replacement of $NADP^+$
325 with NADPH to regenerate the active enzyme for the next reduction reaction.
326

327 **Reaction Mechanism.** LTB_4R reduces a C=C bond that is conjugated with a carbon-oxygen
328 double bond in their substrates. In the reduction reactions catalysed by LTB_4R, the formation
329 of the enolate intermediate was proposed to facilitate the transfer of the hydride ion. As
330 shown in Figure 1, *Vv*CurA also reduces double bonds between C-1 and C-2 atoms and
331 between C-6 and C-7 atoms that are conjugated with the carbonyl double bond. It is thus
332 reasonable to assume the formation of the enolate intermediate during the reaction catalyzed
333 by *Vv*CurA. Hereafter, we only deal with the double bond between C-1 and C-2 atoms

334 because the reduction of the C-1/C-2 double bond is identical to that of the C-6/C-7 double
335 bond due to the symmetrical structure of curcumin. Interestingly, in the *in silico* model of the
336 *Vv*CurA/NADPH/curcumin complex, Tyr251 is hydrogen bonded to the 2′-OH group of the
337 NA-linked ribose, which is 2.7 Å away from the oxyanion in the enolate intermediate (Figure
338 6A). Tyr251 seems to contribute to the stabilization of the enolate intermediate through the
339 2′-OH group-mediated hydrogen bond network (Figure 6A). Consistently, both the Y251F
340 and Y251A mutations significantly reduced the catalytic activity of *Vv*CurA (Figure 6B). The
341 catalytic defect of the isosteric Y251F mutation highlights the importance of the hydroxyl
342 group of Tyr251 that is responsible for the hydrogen bonding.

343 The C-1 atom that is changed to carbocation in the enolate intermediate is 4.2 Å away
344 from the C-4 atom of NADPH (C_{NDP}-4) in the *in silico* model structure (Figure 6A), which
345 indicates that it is well positioned to accept the hydride ion of C_{NDP}-4 during the reaction. For
346 the full reduction of the double bond, the C-2 atom should be protonated. The C-2 atom
347 displaying carbanion character in the enolate intermediate is located inside the active site
348 pocket, which shows that the second proton is less likely to be derived from the solvent.
349 Instead, Tyr62 that is located in the vicinity of the C-2 atom (Figure 6A) is likely to protonate
350 the carbon atom as a general acid catalyst. Both Y62A and Y62F mutations decreased the
351 curcumin-reducing activity (Figure 6B). Compared to the wild-type, the Y62F mutant
352 displayed ~4-fold lowered k_{cat} value (Table 2), which supports the role of the side-chain
353 hydroxyl group in Tyr62 as a proton donor. Arg55 is adjacent to Tyr62 (Figure 6A) and thus
354 its side chain guanidinium group is adequate to stabilize the deprotonated tyrosine residue
355 (tyrosinate) generated after proton donation. Consistently, the R55A mutant showed
356 substantial defect in the curcumin-reducing activity (Figure 6B). Since Arg55, Tyr62, and
357 Tyr251 are conserved in CurA orthologues (Figure S4), we propose the reaction mechanism

358 for curcumin-reducing enzymes (Figure 6C) in which a hydride ion of NADPH is transferred
359 to the C-1 atom in the enolate intermediate that is stabilized by Tyr251 and the protonation of
360 the C-2 atom is achieved by Tyr62 whose acidity is increased by the adjacent Arg55. In this
361 proposed mechanism, the contribution of the solvent for the second protonation cannot be
362 excluded considering the moderate k_{cat} difference between the wild-type and the Y62F mutant.

363

364 ASSOCIATED CONTENT

365 Supporting Information

366 The supporting Information is available free of charge on the ACS Publications website.

367 Figure S1. Metabolites derived from curcumin reduction.

368 Figure S2. Curcumin-reducing activity of CurA depending on temperature and pH.

369 Figure S3. Sequence alignment of *Vibrio vulnificus* CurA with guinea pig LTB_4R.

370 Figure S4. Multiple sequence alignment of CurA orthologues.

371 Table S1. Primer sequences for site-directed mutagenesis.

372 Accession Codes

373 The atomic coordinates and structural factors of the final models of apo *Vv*CurA and
374 *Vv*CurA/NADHP complex have been deposited in the Protein Data Bank with the accession
375 codes 5ZXN and 5ZXU, respectively.

376

377 AUTHOR INFORMATION

Corresponding Authors

S.C. (Tel: +82-2-3277-4503, E-mail: sunchoi@ewha.ac.kr)

M.-K.K. (Tel: +82-63-570-3212, E-mail: mkkim@kaeri.re.kr)

S.-S.C. (Tel: +82-2-3277-3858, E-mail: chajung@ewha.ac.kr)

Author Contribution

¶S.-B.P., D.-W.B, and N.A.B.C contributed equally to this work.

Funding

This work was supported by a grant from Marine Biotechnology Program (20170305, Development of biomedical materials based on marine proteins) funded by Ministry of Oceans and Fisheries, Korea and by National Research Foundation of Korea (NRF) grants funded by the Korean government (MSIT) (NRF-2015M1A5A1037480 and NRF-2017R1A2B4010084).

Notes

The authors declare no competing financial interest.

ACKNOWLEDGMENTS

We thank the beamline staffs at MXII beamline in Australian Synchrotron, Australia, for support with the data collection.

398 **REFERENCES**

399 1. Aggarwal, B. B.; Sundaram, C.; Malani, N.; Ichikawa, H., Curcumin: the Indian solid
400 gold. *Adv Exp Med Biol* **2007,** *595*, 1-75.
401 2. Hatcher, H.; Planalp, R.; Cho, J.; Torti, F. M.; Torti, S. V., Curcumin: from ancient
402 medicine to current clinical trials. *Cell Mol Life Sci* **2008,** *65* (11), 1631-52.
403 3. Aggarwal, B. B.; Kumar, A.; Bharti, A. C., Anticancer potential of curcumin:
404 preclinical and clinical studies. *Anticancer Res* **2003,** *23* (1A), 363-98.
405 4. Huang, Y. T.; Lin, Y. W.; Chiu, H. M.; Chiang, B. H., Curcumin Induces Apoptosis of
406 Colorectal Cancer Stem Cells by Coupling with CD44 Marker. *J Agric Food Chem* **2016,** *64*
407 (11), 2247-53.
408 5. Rudrappa, T.; Bais, H. P., Curcumin, a known phenolic from Curcuma longa,
409 attenuates the virulence of Pseudomonas aeruginosa PAO1 in whole plant and animal
410 pathogenicity models. *J Agric Food Chem* **2008,** *56* (6), 1955-62.
411 6. Masuda, T.; Maekawa, T.; Hidaka, K.; Bando, H.; Takeda, Y.; Yamaguchi, H.,
412 Chemical studies on antioxidant mechanism of curcumin: analysis of oxidative coupling
413 products from curcumin and linoleate. *J Agric Food Chem* **2001,** *49* (5), 2539-47.
414 7. Yang, F.; Lim, G. P.; Begum, A. N.; Ubeda, O. J.; Simmons, M. R.; Ambegaokar, S.
415 S.; Chen, P. P.; Kayed, R.; Glabe, C. G.; Frautschy, S. A.; Cole, G. M., Curcumin inhibits
416 formation of amyloid beta oligomers and fibrils, binds plaques, and reduces amyloid in vivo.
417 *J Biol Chem* **2005,** *280* (7), 5892-901.
418 8. Gupta, S. C.; Patchva, S.; Aggarwal, B. B., Therapeutic roles of curcumin: lessons
419 learned from clinical trials. *AAPS J* **2013,** *15* (1), 195-218.
420 9. Kelloff, G. J.; Crowell, J. A.; Hawk, E. T.; Steele, V. E.; Lubet, R. A.; Boone, C. W.;
421 Covey, J. M.; Doody, L. A.; Omenn, G. S.; Greenwald, P.; Hong, W. K.; Parkinson, D. R.;
422 Bagheri, D.; Baxter, G. T.; Blunden, M.; Doeltz, M. K.; Eisenhauer, K. M.; Johnson, K.;
423 Knapp, G. G.; Longfellow, D. G.; Malone, W. F.; Nayfield, S. G.; Seifried, H. E.; Swall, L.
424 M.; Sigman, C. C., Strategy and planning for chemopreventive drug development: clinical
425 development plans II. *J Cell Biochem Suppl* **1996,** *26*, 54-71.
426 10. Anand, P.; Kunnumakkara, A. B.; Newman, R. A.; Aggarwal, B. B., Bioavailability
427 of curcumin: problems and promises. *Mol Pharm* **2007,** *4* (6), 807-18.
428 11. Kharat, M.; Du, Z.; Zhang, G.; McClements, D. J., Physical and Chemical Stability
429 of Curcumin in Aqueous Solutions and Emulsions: Impact of pH, Temperature, and

430 Molecular Environment. *J Agric Food Chem* **2017,** *65* (8), 1525-1532.
431 12. Peng, S.; Li, Z.; Zou, L.; Liu, W.; Liu, C.; McClements, D. J., Enhancement of
432 Curcumin Bioavailability by Encapsulation in Sophorolipid-Coated Nanoparticles: An in
433 Vitro and in Vivo Study. *J Agric Food Chem* **2018,** *66* (6), 1488-1497.
434 13. Begum, A. N.; Jones, M. R.; Lim, G. P.; Morihara, T.; Kim, P.; Heath, D. D.; Rock, C.
435 L.; Pruitt, M. A.; Yang, F.; Hudspeth, B.; Hu, S.; Faull, K. F.; Teter, B.; Cole, G. M.;
436 Frautschy, S. A., Curcumin structure-function, bioavailability, and efficacy in models of
437 neuroinflammation and Alzheimer's disease. *J Pharmacol Exp Ther* **2008,** *326* (1), 196-208.
438 14. Wang, Y. J.; Pan, M. H.; Cheng, A. L.; Lin, L. I.; Ho, Y. S.; Hsieh, C. Y.; Lin, J. K.,
439 Stability of curcumin in buffer solutions and characterization of its degradation products. *J*
440 *Pharm Biomed Anal* **1997,** *15* (12), 1867-76.
441 15. Priyadarsini, K. I., The chemistry of curcumin: from extraction to therapeutic agent.
442 *Molecules* **2014,** *19* (12), 20091-112.
443 16. Gordon, O. N.; Luis, P. B.; Sintim, H. O.; Schneider, C., Unraveling curcumin
444 degradation: autoxidation proceeds through spiroepoxide and vinylether intermediates en
445 route to the main bicyclopentadione. *J Biol Chem* **2015,** *290* (8), 4817-28.
446 17. Schneider, C.; Gordon, O. N.; Edwards, R. L.; Luis, P. B., Degradation of Curcumin:
447 From Mechanism to Biological Implications. *J Agric Food Chem* **2015,** *63* (35), 7606-14.
448 18. Metzler, M.; Pfeiffer, E.; Schulz, S. I.; Dempe, J. S., Curcumin uptake and
449 metabolism. *Biofactors* **2013,** *39* (1), 14-20.
450 19. Marczylo, T. H.; Steward, W. P.; Gescher, A. J., Rapid analysis of curcumin and
451 curcumin metabolites in rat biomatrices using a novel ultraperformance liquid
452 chromatography (UPLC) method. *J Agric Food Chem* **2009,** *57* (3), 797-803.
453 20. Holder, G. M.; Plummer, J. L.; Ryan, A. J., The metabolism and excretion of
454 curcumin (1,7-bis-(4-hydroxy-3-methoxyphenyl)-1,6-heptadiene-3,5-dione) in the rat.
455 *Xenobiotica* **1978,** *8* (12), 761-8.
456 21. Pan, M. H.; Huang, T. M.; Lin, J. K., Biotransformation of curcumin through
457 reduction and glucuronidation in mice. *Drug Metab Dispos* **1999,** *27* (4), 486-94.
458 22. Mukhopadhyay, A.; Basu, N.; Ghatak, N.; Gujral, P. K., Anti-inflammatory and
459 irritant activities of curcumin analogues in rats. *Agents and actions* **1982,** *12* (4), 508-15.
460 23. Pari, L.; Murugan, P., Antihyperlipidemic effect of curcumin and tetrahydrocurcumin
461 in experimental type 2 diabetic rats. *Renal failure* **2007,** *29* (7), 881-9.
462 24. Sugiyama, Y.; Kawakishi, S.; Osawa, T., Involvement of the beta-diketone moiety in

463 the antioxidative mechanism of tetrahydrocurcumin. *Biochemical pharmacology* **1996,** *52* (4),
464 519-25.
465 25. Osawa, T.; Sugiyama, Y.; Inayoshi, M.; Kawakishi, S., Antioxidative activity of
466 tetrahydrocurcuminoids. *Bioscience, biotechnology, and biochemistry* **1995,** *59* (9), 1609-12.
467 26. Okada, K.; Wangpoengtrakul, C.; Tanaka, T.; Toyokuni, S.; Uchida, K.; Osawa, T.,
468 Curcumin and especially tetrahydrocurcumin ameliorate oxidative stress-induced renal injury
469 in mice. *J Nutr* **2001,** *131* (8), 2090-5.
470 27. Hassaninasab, A.; Hashimoto, Y.; Tomita-Yokotani, K.; Kobayashi, M., Discovery of
471 the curcumin metabolic pathway involving a unique enzyme in an intestinal microorganism.
472 *Proc Natl Acad Sci U S A* **2011,** *108* (16), 6615-20.
473 28. Hedlund, J.; Jornvall, H.; Persson, B., Subdivision of the MDR superfamily of
474 medium-chain dehydrogenases/reductases through iterative hidden Markov model refinement.
475 *BMC Bioinformatics* **2010,** *11*, 534.
476 29. Nordling, E.; Jornvall, H.; Persson, B., Medium-chain dehydrogenases/reductases
477 (MDR). Family characterizations including genome comparisons and active site modeling.
478 *Eur J Biochem* **2002,** *269* (17), 4267-76.
479 30. Kim, M. K.; An, Y. J.; Jeong, C. S.; Cha, S. S., Crystallization and preliminary X-ray
480 crystallographic analysis of the putative NADP(H)-dependent oxidoreductase YncB from
481 *Vibrio vulnificus*. *Acta Crystallogr Sect F Struct Biol Cryst Commun* **2012,** *68* (Pt 9), 1098-
482 101.
483 31. Park, J. H.; Cho, Y. J.; Chun, J.; Seok, Y. J.; Lee, J. K.; Kim, K. S.; Lee, K. H.; Park,
484 S. J.; Choi, S. H., Complete genome sequence of Vibrio vulnificus MO6-24/O. *J Bacteriol*
485 **2011,** *193* (8), 2062-3.
486 32. An, Y. J.; Ahn, B. E.; Roe, J. H.; Cha, S. S., Crystallization and preliminary X-ray
487 crystallographic analyses of Nur, a nickel-responsive transcription regulator from
488 Streptomyces coelicolor. *Acta Crystallogr Sect F Struct Biol Cryst Commun* **2008,** *64* (Pt 2),
489 130-2.
490 33. Kabsch, W., Xds. *Acta Crystallogr D Biol Crystallogr* **2010,** *66* (Pt 2), 125-32.
491 34. Adams, P. D.; Afonine, P. V.; Bunkoczi, G.; Chen, V. B.; Davis, I. W.; Echols, N.;
492 Headd, J. J.; Hung, L. W.; Kapral, G. J.; Grosse-Kunstleve, R. W.; McCoy, A. J.; Moriarty, N.
493 W.; Oeffner, R.; Read, R. J.; Richardson, D. C.; Richardson, J. S.; Terwilliger, T. C.; Zwart, P.
494 H., PHENIX: a comprehensive Python-based system for macromolecular structure solution.
495 *Acta Crystallogr D Biol Crystallogr* **2010,** *66* (Pt 2), 213-21.

496 35. Emsley, P.; Lohkamp, B.; Scott, W. G.; Cowtan, K., Features and development of
497 Coot. *Acta Crystallogr D Biol Crystallogr* **2010,** *66* (Pt 4), 486-501.
498 36. Murshudov, G. N.; Vagin, A. A.; Dodson, E. J., Refinement of macromolecular
499 structures by the maximum-likelihood method. *Acta Crystallogr D Biol Crystallogr* **1997,** *53*
500 (Pt 3), 240-55.
501 37. Winn, M. D.; Ballard, C. C.; Cowtan, K. D.; Dodson, E. J.; Emsley, P.; Evans, P. R.;
502 Keegan, R. M.; Krissinel, E. B.; Leslie, A. G.; McCoy, A.; McNicholas, S. J.; Murshudov, G.
503 N.; Pannu, N. S.; Potterton, E. A.; Powell, H. R.; Read, R. J.; Vagin, A.; Wilson, K. S.,
504 Overview of the CCP4 suite and current developments. *Acta Crystallogr D Biol Crystallogr*
505 **2011,** *67* (Pt 4), 235-42.
506 38. Laskowski, R. A.; MacArthur, M. W.; Moss, D. S.; Thornton, J. M., PROCHECK: a
507 program to check the stereochemical quality of protein structures. *J App Cryst* **1993,** *26* (2),
508 283-291.
509 39. Chen, V. B.; Arendall, W. B., 3rd; Headd, J. J.; Keedy, D. A.; Immormino, R. M.;
510 Kapral, G. J.; Murray, L. W.; Richardson, J. S.; Richardson, D. C., MolProbity: all-atom
511 structure validation for macromolecular crystallography. *Acta Crystallogr D Biol Crystallogr*
512 **2010,** *66* (Pt 1), 12-21.
513 40. Hori, T.; Yokomizo, T.; Ago, H.; Sugahara, M.; Ueno, G.; Yamamoto, M.; Kumasaka,
514 T.; Shimizu, T.; Miyano, M., Structural basis of leukotriene B4 12-
515 hydroxydehydrogenase/15-Oxo-prostaglandin 13-reductase catalytic mechanism and a
516 possible Src homology 3 domain binding loop. *J Biol Chem* **2004,** *279* (21), 22615-23.

517

518

519

520

521

522

523

524 **Figure captions**

525 **Figure 1. Reduction of curcumin.** Structures of curcumin, dihydrocurcumin (DHC), and
526 tetrahydrocurcumin (THC) in the CurA-mediated curcumin reduction metabolism. Double
527 bonds that are reduced are colored in *blue*.

528 **Figure 2. NADPH-dependent curcumin-reducing activity of *Vv*CurA.** (A) NADPH
529 oxidation was monitored at 340 nm in the solution consisting of *Vv*CurA, curcumin, and
530 NADPH. (B) Michealis-Menten graph of wild-type *Vv*CurA. Error bars show the standard
531 deviation of two independent experiments. (C) HPLC analysis of THC generation by *Vv*CurA
532 with curcumin as a substrate.

533 **Figure 3. Overall structure and the dimerization core of *Vv*CurA.** (A) Monomeric
534 structure of the *Vv*CurA/NADPH complex. The nucleotide-binding and catalytic domains are
535 colored in *bright orange* and *pink*, respectively. NADPH is presented as a *deepteal* stick. (B)
536 Dimeric structure of the apo *Vv*CurA. The catalytic domains are colored by *pink* and *skyblue*,
537 and the nucleotide-binding domains are shown in *bright orange* and *smudge*. NADPH is
538 presented as a *deepteal* stick in each monomer. The dimerization core composed of α10
539 helices and β14 strands is indicated by a dotted circle. The active site surrounded by the Y62
540 loop and the α10 helix is indicated by a *blue* ellipse. (C) Sideview of the triangular
541 dimerization core to show hydrophobic interactions in the core. For clarity, only residues in
542 one dimerization motif are labeled. (D) Topview of the core to show polar interactions. *Red*
543 dotted lines indicate interactions between side chains and *black* dotted lines show hydrogen
544 bonding interactions between backbone atoms.

545 **Figure 4. Structural comparison between *Vv*CurA and LTB_4R** (A) Transparent surface
546 presentation of active site pockets of *Vv*CurA and LTB_4R. In the left figure, NADPH and

547 curcumin are from the *in silico* model of the *Vv*CurA/NADPH/curcumin ternary complex. To
548 prepare for the right figure, the structure of guinea pig LTB_4R with $NADP^+$ (PDB code:
549 1V3V) was superposed onto the *in silico* model of the ternary complex. $NADP^+$ in the
550 structure of LTB_4R and curcumin of the *in silico* complex are shown. (B) Superposed
551 structures of guinea pig LTB_4R (*light gray* ribbon) and *Vv*CurA. For emphasis, the Y62 loop
552 and the α10 helix are shown in cartoon.

553 **Figure 5. NADPH binding mode** (A) Residues from the nucleotide-binding and catalytic
554 domains are colored in *bright orange* and *pink*, respectively. Hydrogen bonds between the
555 nucleotide-binding domain and NADPH are presented by *black* dotted lines and *red* dotted
556 lines represent hydrogen bonding interactions between NADPH and the catalytic domain.
557 Dotted lines represent interatomic distances < 3.4 Å indicative of hydrogen bonds or ion pairs.
558 *Gray* spheres are water molecules. (B) The initial $F_o - F_c$ electron-density map contoured at
559 5σ for NADPH in the final model.

560 **Figure 6. Catalytic residues in the active site.** (A) Curcumin binding mode in the *in silico*
561 model. *Purple* and *green* dotted lines represent hydride and proton transfers, respectively,
562 while *black* dotted lines show hydrogen bonds. (B) Relative enzyme activities of wild-type
563 and mutants of *Vv*CurA. (C) Proposed mechanism for curcumin reduction. R represents the
564 2′-monophosphoadenosine-5′-diphosphate group in NADPH. Symmetric part of curcumin is
565 abbreviated as Sym R. Dotted lines represent hydrogen bonds and ion pairs.

566

567

568

569

570 **Tables**

571 **Table 1. Crystallographic Data and Refinement Statistics**

	*Vv*CurA, apo	*Vv*CurA/NADPH complex
PDB code	5ZXN	5ZXU
Data collection		
Beamline	MXII, Australian Synchrotron	MXII, Australian Synchrotron
Wavelength (Å)	0.9791	0.9537
Unit cell	a=90.52, b=91.56, c=104.79 Å	a=b=90.14, c=105.61 Å
Space group	$P2_12_12_1$	$P4_12_12$
Resolution range (Å)	68.95 – 1.85 (1.96 – 1.85)	68.57 – 2.20 (2.32 – 2.20)
Unique reflections	73918 (10339)	22716 (3257)
Redundancy	14.2 (11.6)	11.4 (10.7)
Completeness (%)	99.4 (96.5)	99.9 (100.0)
R_{merge} (%)	1.3 (16.2)	2.4 (33.9)
Average $I/\sigma(I)$	12.5 (1.6)	10.2 (0.8)
Refinement		
Resolution (Å)	19.91 – 1.85 (1.96 – 1.85)	20.05 – 2.20 (2.23 – 2.20)
No. of reflections	73821	22661
R_{work}/R_{free} (%)	20.9/23.6	20.9/23.7
No. of atoms	5509	2709
Protein	5057	2497
NADPH	0	48
MES/Ethylen glycol	60/4	0/0
Water	388	164
B from Wilson plot ($Å^2$)	29.77	44.30

RMS deviation bond lengths (Å)	0.008	0.004
RMS deviation bond angles (deg)	1.085	0.580
Ramachandran plot		
Most favored regions (%)	96.44	93.73
Additional allowed regions (%)	2.96	5.07
[a]Values in parentheses refer to the highest resolution shell.		

572

573 **Table 2. Enzyme kinetic parameters of *Vv*CurA against curcumin.**

***Vv*CurA**	K_M (μM)	V_{max} $(Units\ mg^{-1})$	k_{cat} (min^{-1})
WT	35.52 ± 3.93	9.52 ± 0.48	352.10 ± 17.59
Y62F	21.64 ± 4.79	2.32 ± 0.24	86.03 ± 9.01

574

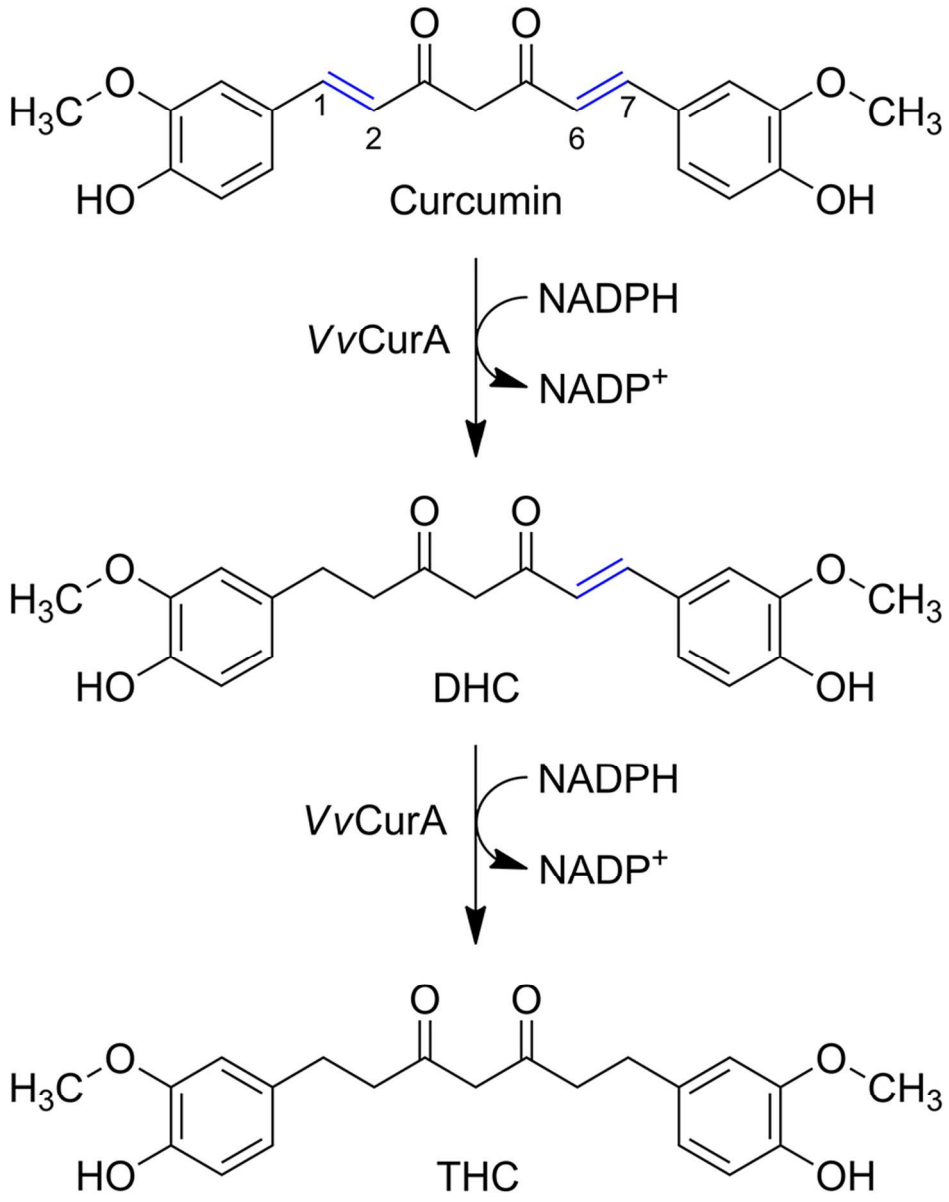

Figure 1. Reduction of curcumin. Structures of curcumin, dihydrocurcumin (DHC), and tetrahydrocurcumin (THC) in the CurA-mediated curcumin reduction metabolism. Double bonds that are reduced are colored in blue.

82x103mm (300 x 300 DPI)

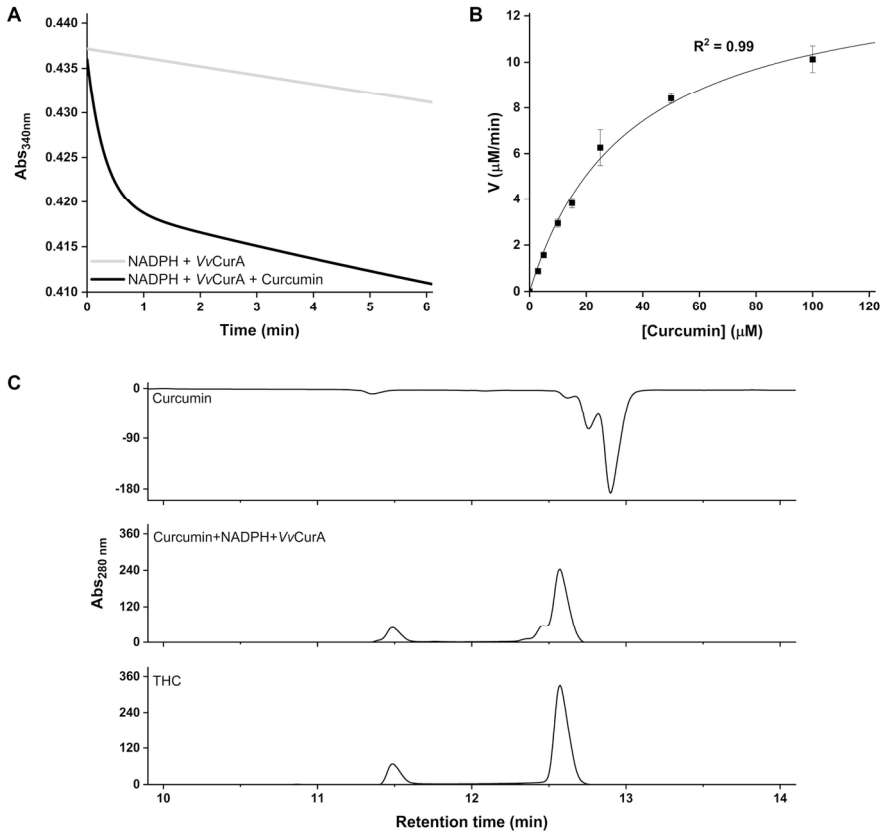

Figure 2. NADPH-dependent curcumin-reducing activity of VvCurA. (A) NADPH oxidation was monitored at 340 nm in the solution consisting of VvCurA, curcumin, and NADPH. (B) Michealis-Menten graph of wild-type VvCurA. Error bars show the standard deviation of two independent experiments. (C) HPLC analysis of THC generation by VvCurA with curcumin as a substrate.

151x129mm (300 x 300 DPI)

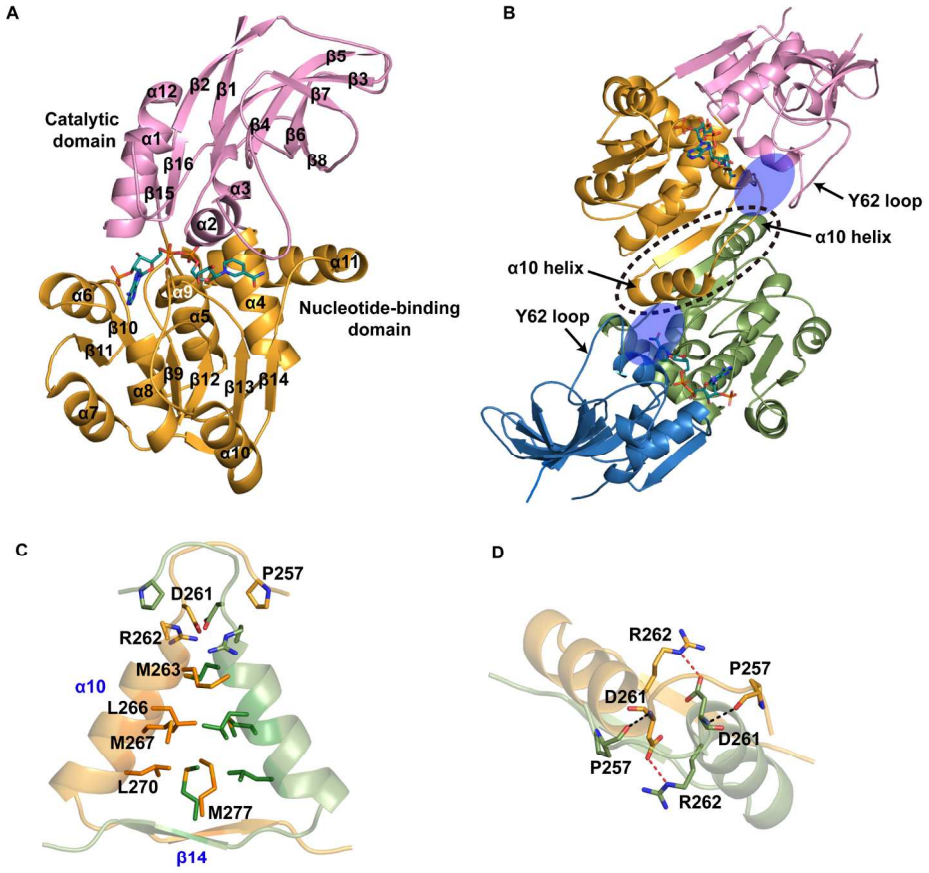

Figure 3. Overall structure and the dimerization core of VvCurA. (A) Monomeric structure of the VvCurA/NADPH complex. The nucleotide-binding and catalytic domains are colored in bright orange and pink, respectively. NADPH is presented as a deepteal stick. (B) Dimeric structure of the apo VvCurA. The catalytic domains are colored by pink and skyblue, and the nucleotide-binding domains are shown in bright orange and smudge. NADPH is presented as a deepteal stick in each monomer. The dimerization core composed of α10 helices and β14 strands is indicated by a dotted circle. The active site surrounded by the Y62 loop and the α10 helix is indicated by a blue ellipse. (C) Sideview of the triangular dimerization core to show hydrophobic interactions in the core. For clarity, only residues in one dimerization motif are labeled. (D) Topview of the core to show polar interactions. Red dotted lines indicate interactions between side chains and black dotted lines show hydrogen bonding interactions between backbone atoms.

194x194mm (300 x 300 DPI)

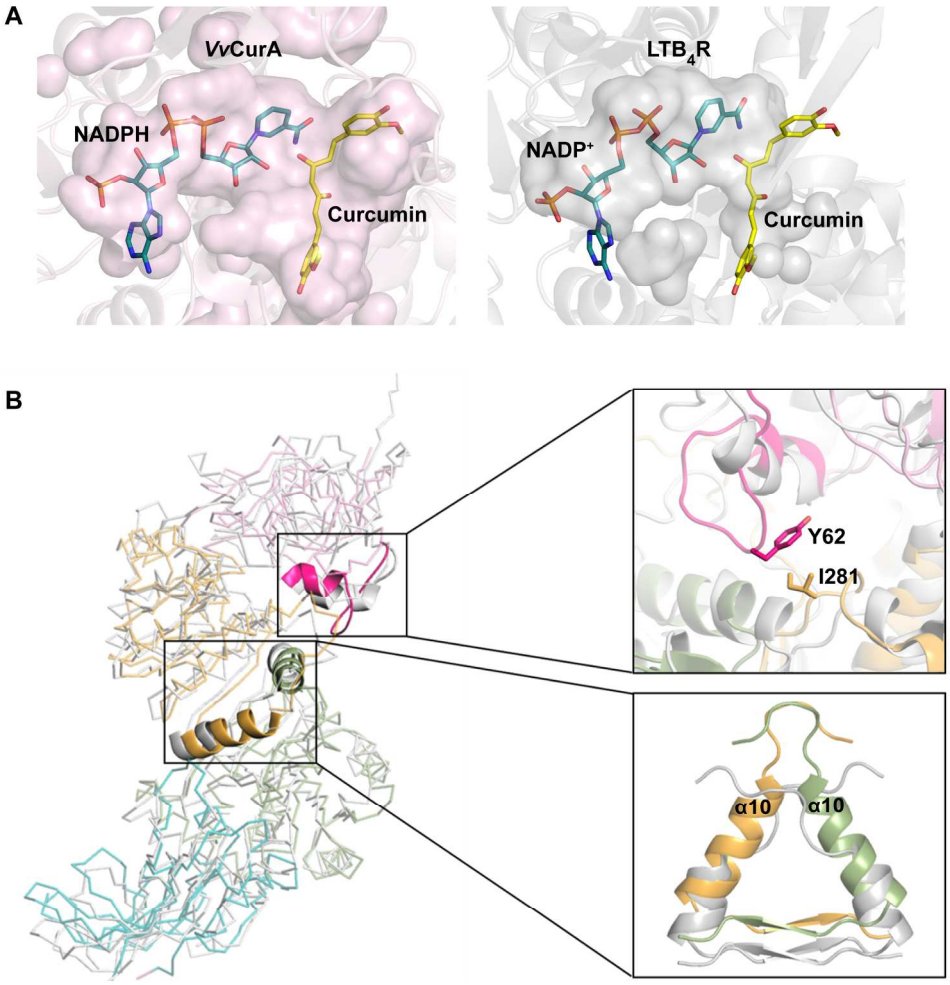

Figure 4. Structural comparison between VvCurA and LTB4R (A) Transparent surface presentation of active site pockets of VvCurA and LTB4R. In the left figure, NADPH and curcumin are from the in silico model of the VvCurA/NADPH/curcumin ternary complex. To prepare for the right figure, the structure of guinea pig LTB4R with NADP+ (PDB code: 1V3V) was superposed onto the in silico model of the ternary complex. NADP+ in the structure of LTB4R and curcumin of the in silico complex are shown. (B) Superposed structures of guinea pig LTB4R (light gray ribbon) and VvCurA. For emphasis, the Y62 loop and the α10 helix are shown in cartoon.

197x204mm (300 x 300 DPI)

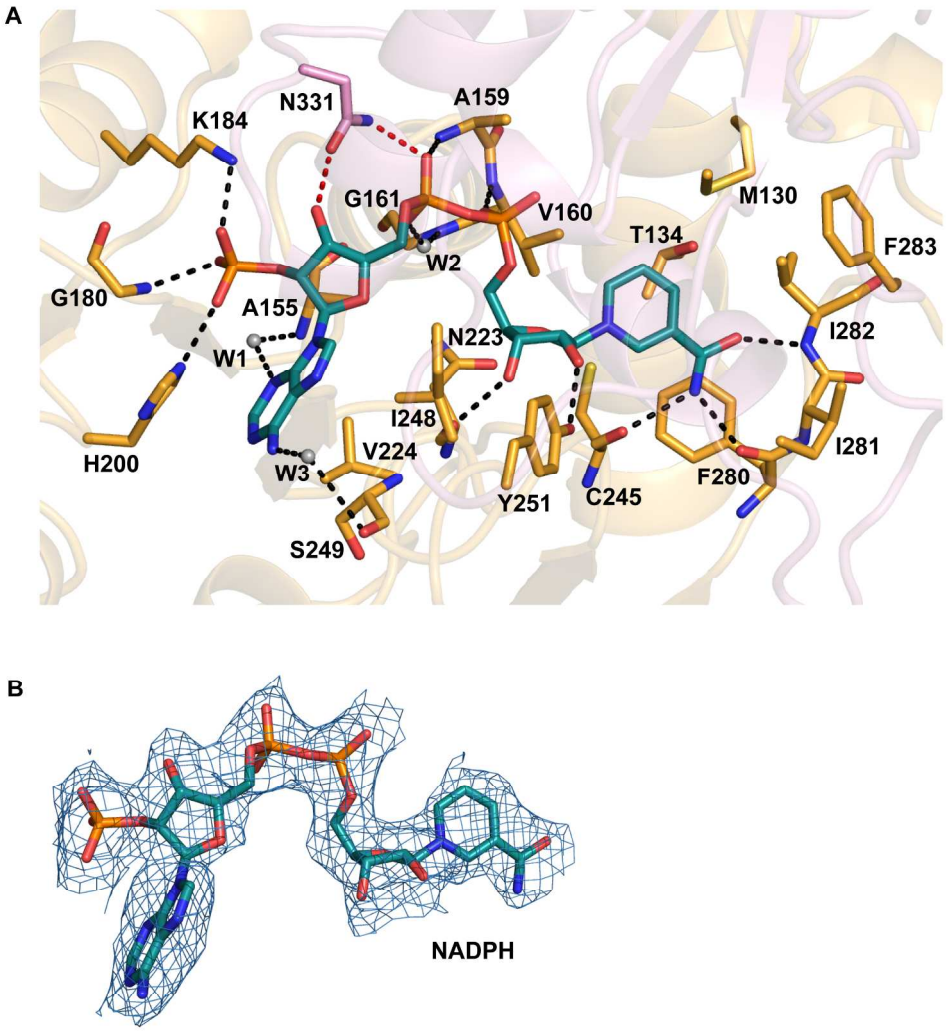

Figure 5. NADPH binding mode (A) Residues from the nucleotide-binding and catalytic domains are colored in bright orange and pink, respectively. Hydrogen bonds between the nucleotide-binding domain and NADPH are presented by black dotted lines and red dotted lines represent hydrogen bonding interactions between NADPH and the catalytic domain. Dotted lines represent interatomic distances < 3.4 Å indicative of hydrogen bonds or ion pairs. Gray spheres are water molecules. (B) The initial Fo – Fc electron-density map contoured at 5σ for NADPH in the final model.

210x239mm (300 x 300 DPI)

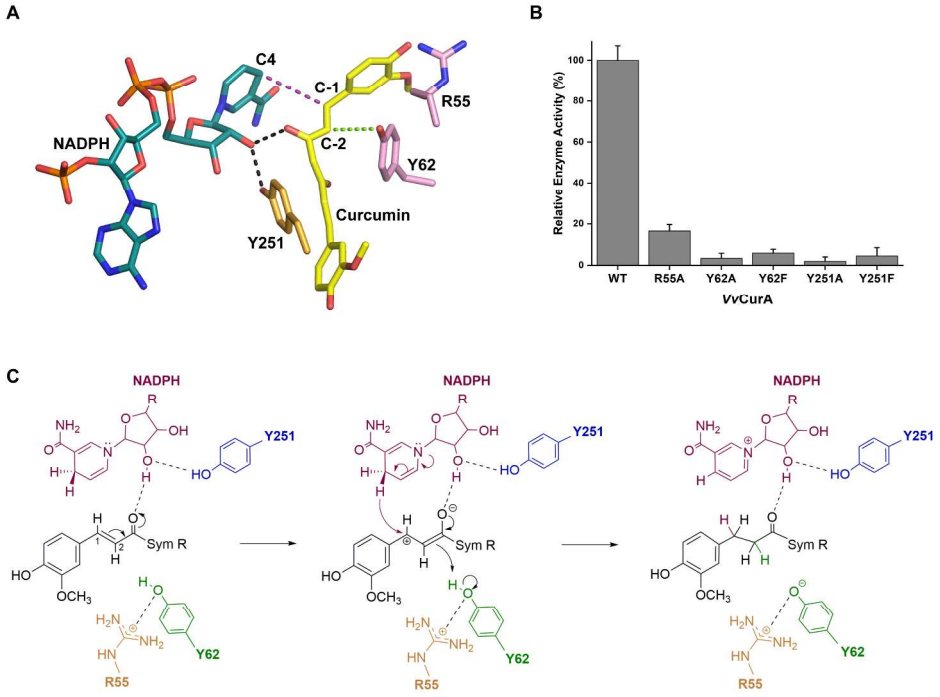

Figure 6. Catalytic residues in the active site. (A) Curcumin binding mode in the in silico model. Purple and green dotted lines represent hydride and proton transfers, respectively, while black dotted lines show hydrogen bonds. (B) Relative enzyme activities of wild-type and mutants of VvCurA. (C) Proposed mechanism for curcumin reduction. R represents the 2′-monophosphoadenosine-5′-diphosphate group in NADPH. Symmetric part of curcumin is abbreviated as Sym R. Dotted lines represent hydrogen bonds and ion pairs.

264x194mm (300 x 300 DPI)

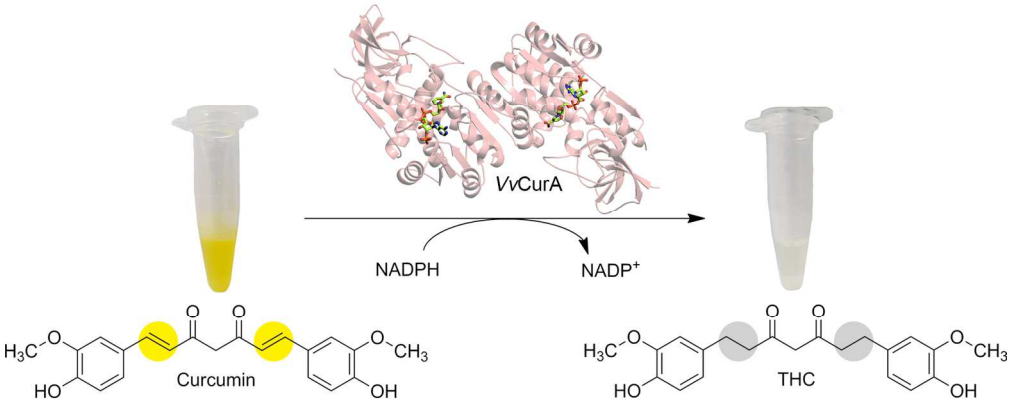

Graphic for table of contents

177x74mm (300 x 300 DPI)